Boosting the bifunctional oxygen electrocatalytic performance of atomically dispersed Fe site via atomic Ni neighboring

Mang Ma[a], Anuj Kumar[d], Danni Wang[b], Yiyan Wang[a], Yin Jia[c], Ying Zhang[a], Guoxin Zhang[b,*], Zifeng Yan[a], Xiaoming Sun[a,c,**]

[a] State Key Laboratory of Heavy Oil Processing, China University of Petroleum (East China), Qingdao, Shandong 266580, PR China
[b] Department of Electrical Engineering and Automation, Shandong University of Science and Technology, Qingdao, Shandong 266590, PR China
[c] State Key Laboratory of Chemical Resource Engineering, Beijing University of Chemical Technology, Beijing 100029, PR China
[d] Department of Chemistry, Institute of Humanities and Applied Science, GLA University, Mathura 281406, India

ABSTRACT

Atomically dispersed metal-nitrogen-carbon complexes on carbon supports have drawn tremendous attention in the electrocatalysis fields. Herein, we managed the synthesis of atomically dispersed binary Ni_xFe_{100-x}-NC (x = 0–100) materials with tunable Ni/Fe ratios and investigated their underneath synergy effects for the enhancement of oxygen reduction (ORR) and oxygen evolution reactions (OER). EXAFS revealed the abundant presence of $Ni(N_3)$-$Fe(N_3)$-C_n moieties in $Ni_{66}Fe_{34}$-NC sample. XPS fine scans indicated deep synergy of dual-site Ni/Fe that favored more charge localized over Ni/Fe sites. Electrochemical measurments showed that the $Ni_{66}Fe_{34}$-NC delivered a very high ORR half-wave potential ($E_{1/2}$) of 0.85 V and a low OER overpotential of 467 mV at ~10 mA cm^{-2} ($Ej = 10$). The Fe site with Ni neighboring, as suggested by DFT simulations and *in-situ* Raman, was the responsible site for both ORR and OER. Furthermore, the $Ni_{66}Fe_{34}$-NC-assembled Zn-air battery afforded large specific power density and extraordinary cycling stability.

1. Introduction

The increasing energy demand and environmental concern associated with the use of fossil fuels have forced the modern society for the inclusive researches to recognize economical, sustainable, and eco-friendly energy technologies such as fuel cells [1,2], metal-air batteries [3,4], and water electrolyzers [5,6]. The two key reactions: oxygen reduction reaction (ORR) and oxygen evolution reaction (OER) in these energy technologies involve multistep proton-coupled electron transfer processes, forging sluggish kinetics that severely constrain the development of clean energy utilization technologies [7–10]. In this context, the noble metal-based materials such as Pt, Ru, Ir were anticipated as practical solutions but their low natural reserves and high costs significantly impeded the commercialization of these technologies at large scale [11,12]. Therefore, there are urgent demands of low-cost, eco-friendly and high-performance electrocatalytic materials to replace the noble metal-based catalysts for the development of next-generation energy utilization technologies [13,14]. The atomically dispersed metal-nitrogen-carbon (M-N-C) materials represent a typical sort of

state-of-the-art electrocatalytsts for the bifunctional ORR/OER electrocatalysis [15,16]. Though, newly emerged, this novel class of materials have gained increasing attention due to their unique atomic structures and strong metal-substrate interactions. More importantly, they allow the utilization of non-precious metal precursors for obtaining comparable catalytic performance relative to noble metal-based catalysts in broad catalysis fields such as ORR [17–19], OER [20,21], hydrogen evolution reaction [22–24], carbon dioxide reduction [25,26], nitrogen reduction [27,28], polysulfide conversion [29,30], and uniform Li ion plating [31], etc.

In view of the published theoretical and experimental reports on N_4-macrocycles [32] and atomically dispersed M-N-C materials [33–35], the extraordinary catalytic activity of M-N-C materials is mainly associated with the co-existence of atomic metal center and the beneficial N_x surroundings, by virtue of electron density sharing via the M-N-C bond linking [36,37]. It is believed that the metal-nitrogen-carbon bonded moieties cooperatively act as the responsible sites to facilitate the multistep proton-coupled electron transfer processes in ORR/OER [38–40]. The interaction of the centered metal site with functional

---

surrounding can be mediated by ways of local heteroatom doping [41,42], defect engineering [43,44], and dual-site formation [45,46], etc. Among them, the formation of metal-metal dual sites not only favors the cost/time-efficient assembly of integrated energy utilization devices [47–49],but also significantly boosts electrocatalytic performance by virtue of inventing more efficient catalytic route compared to single-site M-N-C [50,51]. The past few years have wintessed the fruitful achievements of dual-site atomically dispersed M-N-C materials for exceptional enhancement in ORR by Fe-Co [52], Fe-Mn [53], Fe-Fe [54], and Co-Zn [55] dimers and OER by Ni-Co [56,57] and Ni-Fe [58] dimers. Nevertheless, very few papers have addressed the preparation of bifunctional atomically dispersed dual-site NiFe-N-C materials for reversible OER and ORR, and the identification of roles of Fe and Ni during electrocatalytic processes.

In this study, we developed an efficient method for the synthesis of atomically dispersed binary NiFe-NC materials with tunable Ni/Fe ratios. EXAFS results confirmed the atomic dispersion of Ni/Fe components in the NiFe-NC material with an optimal Ni/Fe ratio of 66:34 (termed as $Ni_{66}Fe_{34}$-NC) with detailed structure of dual-site $Ni(N_3)$-Fe (N_3)-C_n. Strong synergistic interaction between Ni and Fe was revealed by XPS fine scans and validated by computational simulations, confirming the dual-site mode of Ni-Fe dimers beneficial for accumulating electron density in localized area of $Ni(N_3)$-$Fe(N_3)$-C_n. The $Ni_{66}Fe_{34}$-NC showed lower overpotential gap (ΔE) of 0.849 V between ORR half-wave potential ($^{ORR}E_{1/2}$) and OER overpotential of 467 mV at 10 mA cm^{-2} ($^{OER}Ej = 10$), as compared to the mixture of noble metal-based Pt/C and RuO_2 catalysts ($\Delta E = 0.911$ V). Furthermore, the DFT simulations and *in-situ* Raman characterizations indicated that the Fe site in $Ni(N_3)$-$Fe(N_3)$-C_n, after Ni site being saturated by OH, was the responsible site for both ORR and OER. Furthermore, the $Ni_{66}Fe_{34}$-NC-assembled air cathode showed excellent rechargeable Zn–air battery (ZAB) performance, affording a large power density (~ 140.1 mW cm^{-2}) and extraordinary cycling stability (stably cycled for 1000 cycles at high rate of 20.0 mA cm^{-2}). In addition, our developed method should be applicable for the synthesis of other types of atomically dispersed dual-site MM-N-C materials for the investigations of broad electrocatalysis.

2. Experimental

2.1. Materials

Analytical grade zinc chloride ($ZnCl_2$), nickel chloride ($NiCl_2$), ferrous chloride ($FeCl_2$),were obtained from Aladdin Industrial Corporation. Formamide (FA, A.R. grade) was purchased from Xilong Chemical Co., Ltd. The commercial Pt/C catalyst (20 wt.%, ~ 3 nm Pt nanoparticles on Vulcan XC-72 carbon support) and Nafion solution (~ 5 wt.%) were purchased from Sigma-Aldrich Co., LTD. All chemicals were of commercial grade and used without further purification.

2.2. Preparation of atomically dispersed NiFe-NC with tunable Ni/Fe ratios

For the synthesis of Ni_xFe_{100-x}-NC, the total concentration of metal ions (including Ni, Fe, Zn) was maintained at 1.0 mol L^{-1}, and the molar ratio of Zn to Ni/Fe in 9:1. Keeping the quantity of Zn constant, ratio of Ni/Fe was regulate to optimize atomic concentration. Nickel chloride ($NiCl_2$), ferrous chloride ($FeCl_2$), and zinc chloride ($ZnCl_2$) were added into 40.0 mL of FA. The mixture was heated and sonicated for 0.5 h to obtain a homogeneous solution. Then the solution was transferred into a 50.0 mL Teflon-lined autoclave and heated at 180 ℃ for 12 h. The resulted black product was purified with deionized water for 3 times and ethanol solution for 2 times. The obtained products were dried at 80 ℃ overnight and collected without any post-treatment, named as pre-Ni_xFe_{100-x}-NC. pre-Ni_xFe_{100-x}-NC was placed in the ceramic boat and heated at 900 ℃ with a heating rate of 5 ℃ min^{-1} for 1 h in a tube furnace under flowing N_2. The black product after annealing was collected without any post-treatment and named as

Ni_xFe_{100-x}-NC.

2.3. Characterizations

The morphology and microstructures of the samples were examined by transmission electron microscopy (JEM-2100UHR, JEOL). High-resolution transmission electron microscopy (HRTEM, operated at 200 kV) images were recorded using a JEOL 2100 high-resolution transmission electron microscope. Aberration-corrected high-angle annular darkfield scanning transmission electron microscope (HAADF-STEM) images and element mapping images were recorded on a JEOL JEM-ARM200 F TEM/STEM with a spherical aberration corrector (operated at 200 kV). The powder XRD patterns of the samples were performed on a PANalytical X-ray diffraction meter with Cu Kα radiation at a scan rate of 10 ℃ min^{-1} in the 2θ range from 5 to 75°. The surface functional group was studied by X-ray photoelectron spectroscopy (XPS, Thermo Scientific Escalab 250XI). The C1s line at 284.3 eV was utilized as a reference for the binding energies in the acquired spectra. Based on the Shirley-type background, all the high-resolution XPS spectra were deconvoluted via the peak components represented by an 80 % Gaussian-20 % Lorentzian function. Raman spectroscopy (LabRAM ARAMIS, excited with a 532 nm laser).

2.4. Electrochemical measurements

Electrochemical measurement was conducted using a three-electrode test system consisting of platinum electrode as counter electrode, saturated calomel electrode (SCE) as reference electrode, and glassy carbon electrode (GCE) electrode modified with different catalyst samples as working electrode. In 0.1 mol L^{-1} KOH aqueous electrolyte, electrochemical workstation (Chenhua CHI 760E) was used for the tests at room temperature. Catalyst ink was prepared according to typical preparation methods: 5.0 mg catalyst, 1.0 mg carbon black and 10.0 uL Nafion solution (5 wt.%) were added in 0.50 mL ethanol, followed by ultrasonication for 0.5 h to form a homogeneous catalyst ink. For the catalyst film deposited on the glassy carbon electrode (GCE), catalyst load of 0.25 mg cm^{-2} was formed by evenly dropping 5.0 uL catalyst ink onto the polished glass carbon rotary disc electrode (RDE, surfae area ~ 0.196 cm^{-2}). For comparison, reference electrocatalysts Pt/C for ORR and RuO_2 for OER were prepared by the same method with the same mass loading. Before measurements, O_2 was bubbled into the electrolyte for at least 30 min to have O_2 saturation. The scanning rate of CV was 100 mV s^{-1}. The ORR polarization curves measured by RDE were obtained by using linear scanning voltammetry at speeds of 400, 625, 900, 1225, 1600 and 2025 rpm with scan rate of 5.0 mV s^{-1}. OER polarization curves measured by RDE were obtained at a rotation speed of 1600 rpm and scan rate at 5.0 mV s^{-1}. All the potentials in this work are referenced to the reversible hydrogen electrode (RHE). The transfer electron number (n) was calculated by the Koutechy–Levich (K–L) equation:

$$\frac{1}{J} = \frac{1}{J_L} + \frac{1}{J_K} = \frac{1}{B\omega^{1/2}} + \frac{1}{J_K} \qquad (1)$$

$$B = 0.62nF(D_0)^{2/3}\upsilon^{-1/6}C_0 \qquad (2)$$

where J is the measured current density, J_K and J_L are the kinetic and limiting current densities, ω is the rotation rate, ν is the kinetic viscosity of the electrolyte (0.01 cm^2 S^{-1} for 0.1 mol L^{-1} KOH solution), F is the Faraday constant ($F = 96485$ C mol^{-1}), C_0 is the concentration of O_2 (1.2×10^{-3} mol L^{-1} for 0.1 mol L^{-1} KOH solution), D_0 is the diffusion coefficient of O_2 (1.93×10^{-5} cm^2 s^{-1} for 0.1 mol L^{-1} KOH solution). Tafel slopes were calculated using the data of the LSV profiles using Tafel equation:

$$\eta = a + b \times \log|j| \qquad (3)$$

where η is the overpotential, j is the disk current density, and b is the

Tafel slope. The electrochemical stability of the catalysts was evaluated by using the long chronoamperometry measurements at -0.6 V for ORR and at 0.6 V for OER with rotation speed of 1600 rpm. Electrochemical surface area (ECSA) was determined by cyclic voltammetry collected with different scan rates (10, 20, 30, 40, 50, 60, 70, 80, 90 and 100 mV s^{-1}) in a fixed scan window form 0 to 0.05 V vs. SCE, as experimentally studied previously, electrocatalysts with higher double-layer capacitance (C_{dl}) possess larger ECSA. C_{dl} was determined using CV with and a series of scan rates by plotting the capacitive current versus scan rate and performing a linear fit.
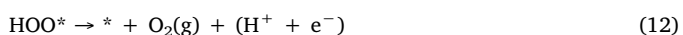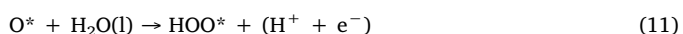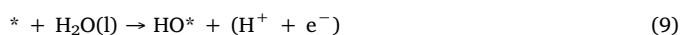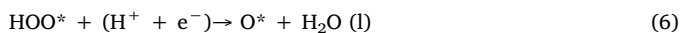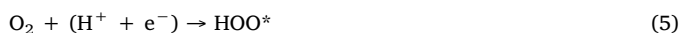
2.5. Rechargeable Zn–air battery assembly

The performance of rechargeable zinc-air battery (ZAB) was analyzed on a self-assembled electrochemical cell. Zinc plate (dimensions of 85 × 34 × 0.5 mm^3) is used as anode. The air cathode is composed of a hydrophobic gas diffusion layer (GDL) and a hydrophilic catalyst layer (Ni_xFe_{1-x}-NC or 1:1 w/w mixed Pt-C/RuO$_2$ catalyst-coated carbon paper) with catalyst loading of 1.0 mg cm^{-2}. The catalyst ink was prepared by mixing carbon black and catalyst (1:5 w/w) in an ethanol:Nafion (50:1 v/v) solution. 6.0 mol L^{-1} KOH solution containing 0.2 mol L^{-1} Zn(OAC)$_2$ was used as electrolyte. All ZAB cells were evaluated under atmospheric conditions. The static discharge and charging voltage characteristics were tested on the terrestrial CT2001A multi-channel battery test system. The specific capacity was measured by a constant current discharge of 10 mA cm^{-2}, and then the mass of Zn plate was measured before and after the measurement. The power density was determined by the product of the discharge voltage and the discharge current in the expression of P = V × I.

2.6. Computational methods and models

All the first-principle simulation results on the structures were obtained by using the Vienna Ab-initio simulation package (VASP), according to the density functional theory (DFT) [59–61]. The projector-augmented wave (PAW), the generalized gradient approximation with Perdew-Burke-Emzerhof (GGA-PBE) were employed to describe the ion-electron interactions and the exchange-correlation potential [62,63].With respect to 3d transitional metals (Ni and Fe), they were correspondingly conferred by the U-J values of 3.40 and 3.29 to provide more accurate energetics [61]. During all the process of calculations, a plane-wave basis was utilized with a kinetic cut-off energy of 500 eV. All atoms were relaxed until the total energy was converged to 1.0*10^{-5} eV and the force was less than 0.01 eV per atom. A (3 × 3 × 1) k-point sampling was generated through the Monkhorst-Pack method. Particularly, it was increased to (5 × 5 ×1) for the sack of electronic structure calculations. All single-atom metal-nitrogen-carbon catalysts were modeled as three-dimensional periodic structures with the vacuum layers of around 15 Å in the z-direction [64].

The two opposite processes of ORR (4–8) and OER (9–12) include several elementary steps as followed [65]:

$$O_2 + * \rightarrow O_2* \tag{4}$$

$$O_2 + (H^+ + e^-) \rightarrow HOO* \tag{5}$$

$$HOO* + (H^+ + e^-) \rightarrow O* + H_2O \text{ (l)} \tag{6}$$

$$O* + (H^+ + e^-) \rightarrow HO* \tag{7}$$

$$HO* + (H^+ + e^-) \rightarrow * + H_2O \tag{8}$$

$$* + H_2O(l) \rightarrow HO* + (H^+ + e^-) \tag{9}$$

$$HO* \rightarrow O* + (H^+ + e^-) \tag{10}$$

$$O* + H_2O(l) \rightarrow HOO* + (H^+ + e^-) \tag{11}$$

$$HOO* \rightarrow * + O_2(g) + (H^+ + e^-) \tag{12}$$

where *, HOO*, O* and HO* denote to the active sites on the surface of catalysts and adsorbed intermediates. In accordance with computational hydrogen electrode (CHE) model, the potential of (H$^+$ + e$^-$) can be substituted by the half of the free energy of the hydrogen. The energy difference between the initial and finial states, △G, is expressed by the following equation [66]:

$$\triangle G = \triangle E_{ads} + \triangle ZPE - T\triangle S - eU - k_BT \ln[H^+] \tag{13}$$

where E_{ads}, ZPE, T, S, e and U represent for the total energy, the zero-point energy, temperature, entropy, charge and potential at the electrode.

The overpotentials (η) are given by the expression [67]:

$$\eta_{ORR} = \triangle G_{max}/e - 1.23 \text{ V} \tag{14}$$

$$\eta_{OER} = \triangle G_{min}/e - 1.23 \text{ V} \tag{15}$$

3. Results and discussion

The atomically dispersed bi-metal Ni_xFe_{100-x}-NC (x = 0–100) materials were obtained by two consecutive steps; solvothermal treatment of Ni/Fe/Zn salts in formamide (FA) and inert annealing treatment of NiFeZn-NC precursor. FA, containing 26.7 wt.% C and 31.1 wt.% N, was used as N/C source. Formamide (FA) was employed as both carbon and nitrogen sources, as previously studied, FA can be self-condensed and carbonized into heavy N-containing carbon materials [68]. The N content of resulted N-doped carbonaceous materials obtained via solvothermal treatment can reach up to ~30.2 at.%, which is the prerequisite for the stabilization of dense metal atoms at high temperature. Additionally, Zn components, as reliable fencing agents, are reducible and vaporizable at high temperatures and can be served as the secondary agents for the immobilization of active metal atoms [69–72]. XRD profile (Fig. 1a) of bi-metallic pre-$Ni_{66}Fe_{34}$-NC sample showed a typical phase of zinc iron cyanide resembling with pre-Fe-NC, while pre-Ni-NC exhibits amorphous phase which was mainly due to the catalysis of Fe species for the dehydration of FA into cyanide groups and water [73].

The SEM (Fig. 1b) and TEM (Figure S1a) images of pre-$Ni_{66}Fe_{34}$-NC sample displayed the typical flower-like morphology assembled by thin zinc iron cyanide nanosheets. The HRTEM (Figure S2b) and elemental mapping (Fig. 1c) images of pre-$Ni_{66}Fe_{34}$-NC sample confirm the uniform distribution of Ni, Fe, and Zn components without any metallic aggregation. It can be ascribed to the promotion of Zn fencing and rich N loading [49].Further, XPS was performed to examine the chemical states of metallic species in pre-$Ni_{66}Fe_{34}$-NC sample and compared with pre-Fe-NC and pre-Ni-NC samples. As displayed in Figure S1c, the XPS elemental survey of pre-$Ni_{66}Fe_{34}$-NC sample exemplifies the six signals corresponding to C (~285 eV), O (~533 eV), N (~400 eV), Zn (~1100 eV), Fe (~710 eV), and Ni (~855 eV). Remarkably, N and Zn contents were reached close to 36.0 at.% and 5.2 at.%, respectively. XPS fine scan on N1s spectra (Figure S1d) reveals over 93.5 % N species in anchorable pyridinic and pyrrolic N forms which can facilitate the immobilization of Ni and Fe atoms in carbon matrix [49,74–76].The Ni and Fe components, as finely scanned and deconvoluted in Figure S1e/f, were identified with their usual oxidation states, suggesting their atomic dispersion on heavy N/Zn-loaded carbon substrate under the metal-nitrogen coordination driving force. It is noticeable that the binding energy of both Ni2p and Fe2p states of pre-$Ni_{66}Fe_{34}$-NC sample exhibit down-shifting phenomenon compared to those of pre-Fe-NC and pre-Ni-NC (Figure S1e/f), respectively, which can be ascribed to its synergistic interaction between Ni and Fe atoms.

Pyrolysis of pre-Ni_xFe_{100-x}-NC sample at 900℃ enabled the removal of unstable N-containing carbon fragments and vaporizable Zn component, leading the graphitization of materials and immobilization of Ni/Fe atoms by multiple N bonding [70,71,77]. In this way, a series of Ni_xFe_{100-x}-NC materials (x = 0–100) with different Ni to Fe ratios was
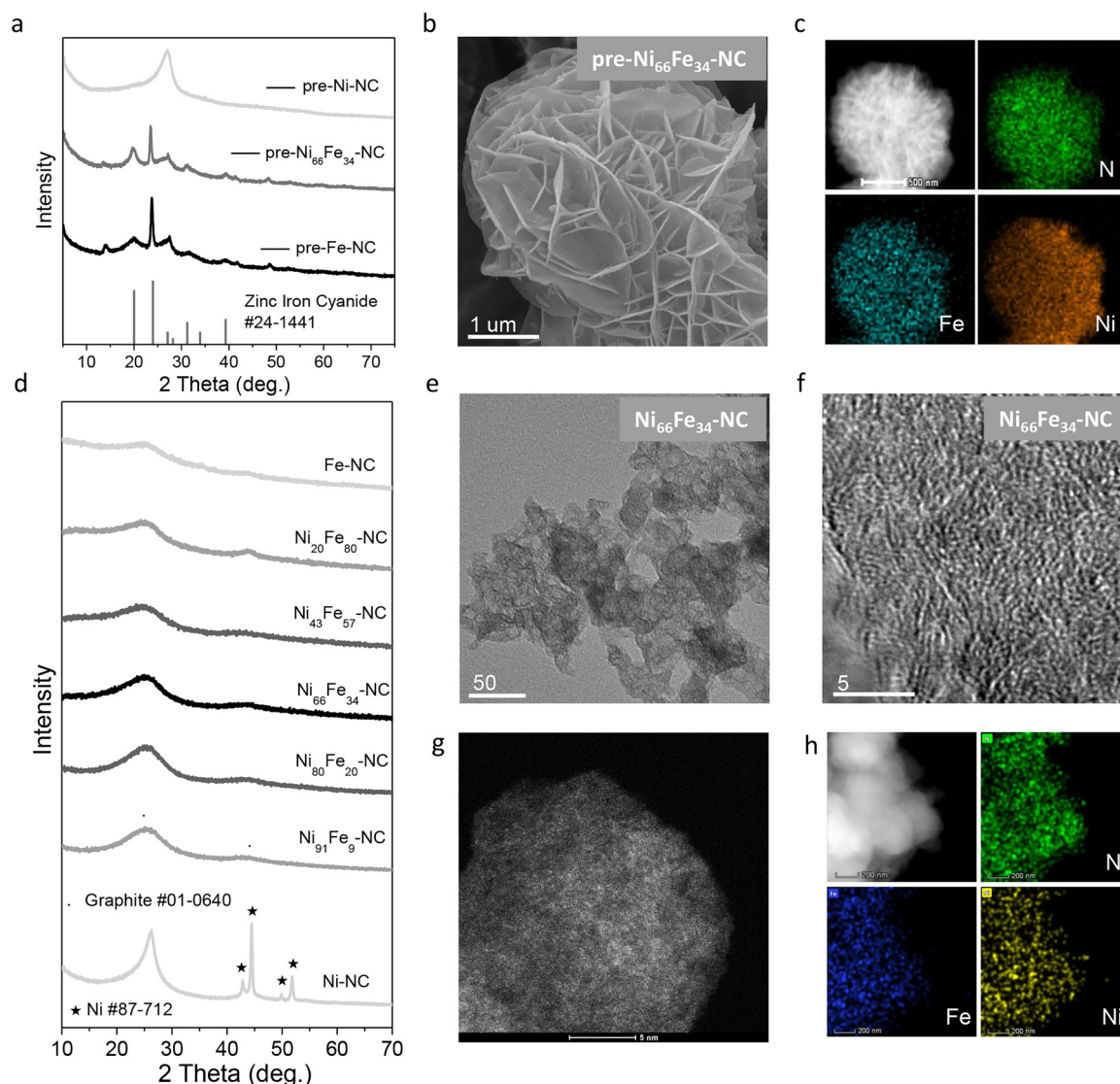
Fig. 1. (a) XRD profiles of pre-Ni-NC, pre-$Ni_{66}Fe_{34}$-NC, and pre-Fe-NC.(b) SEM image of pre-$Ni_{66}Fe_{34}$-NC. (c) HADDF-STEM and elemental mapping images of pre-$Ni_{66}Fe_{34}$-NC. (d) XRD profiles of Ni_xFe_{1-x}-NC, x = 91, 80, 66, 43, 20, 0. (e) TEM images of $Ni_{66}Fe_{34}$-NC. (f) HRTEM image of $Ni_{66}Fe_{34}$-NC. (g) Zoom-in HAADF-STEM image of $Ni_{66}Fe_{34}$-NC. (h) HAADF-STEM and element mapping images of $Ni_{66}Fe_{34}$-NC.

synthesized by following same protocol to investigate the cooperative effect between Ni and Fe atoms, and to explore the optimal ratio of Ni to Fe for the excellent bifunctional ORR/OER activities. Initially, the dispersion of active Ni and Fe components was examined by using XRD, as shown in Fig. 1d, high dispersion can be achieved with broad x = 0, 20, 43, 66, 80, and 91, indicating the amorphous state of carbonaceous materials in Ni_xFe_{100-x}-NC materials. The Ni-NC material is exceptive, consisting of graphitic carbon and Ni nanocrystals, as indicated by the typical lattices indexed to graphite and Ni substance, respectively. The morphologies and phases of Ni_xFe_{100-x}-NC materials were further examined by using TEM, as shown in Fig. 1e and Figure S2, all the Ni_xFe_{100-x}-NC materials exhibit irregularly shaped morphologies. The collapse of flower-like morphology and transformation into irregularly shaped porous morphology was probably due to the destruction caused by the removal of large amount of N-containing carbon fragments and Zn component [49,72]. The TEM image (Figure S2a) of Ni-NC confirms its presence of Ni nanoparticles, which is in agreement with XRD analysis. The Raman spectra (Figure S3) of Ni_xFe_{100-x}-NC materials indicated high extents of defect degree in all Ni_xFe_{100-x}-NC by showing a narrow range of high I_D/I_G ratios from 1.02 to 1.11, which was probably attributed to the heavily loaded N/Ni/Fe-containing moieties

[78,79].

Typically, the $Ni_{66}Fe_{34}$-NC material was submitted to HRTEM and aberration-corrected atomic-resolution high-angle annular dark field scanning transmission electron microscopy (HAADF-STEM) to reveal the microstructures and the dispersions of metallic components. Fig. 1f confirms the short-range graphitization of $Ni_{66}Fe_{34}$-NC by displaying the clear lattice planes, which are in agreement with the G band in its Raman spectra, meanwhile, no crystallized particle or cluster is observed, as supported by XRD analysis (Fig. 1d). The HAADF-STEM image in Fig. 1g exhibits dense bright dots randomly distributing in $Ni_{66}Fe_{34}$-NC, typifying the atomic dispersion of Ni and Fe component. In addition, the atomic Ni and Fe species along with dense N loading are also confirmed by their uniform distributions in $Ni_{66}Fe_{34}$-NC, as revealed by the element mapping images in Fig. 1h. Furthermore, XPS was employed to analyze the elemental states of Ni_xFe_{100-x}-NC materials. Figure S4 exhibits the XPS elemental survey of all Ni_xFe_{100-x}-NC materials, in which the Ni_xFe_{100-x}-NC materials (x = 20, 43, 66, 80, and 91) display the co-presence of C, O, N, Zn, Ni, and Fe. The carbon contents of Ni_xFe_{100-x}-NC materials with co-existance of Ni and Fe fall in the range of 73.3–75.6 at.% (Table S1), which are lower than those of Ni-NC and Fe-NC materials. In contrast, the N and Zn contents of
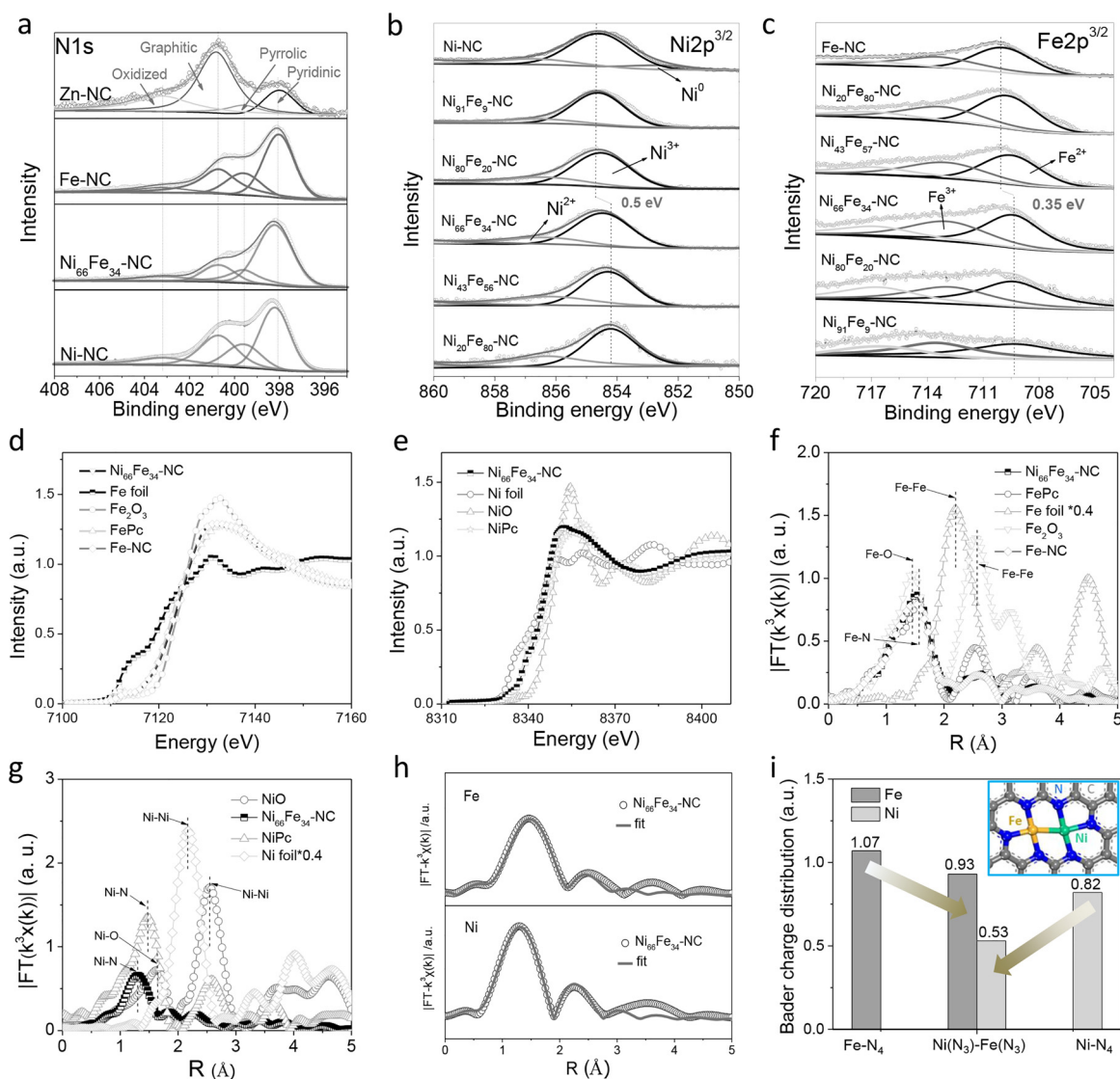
Fig. 2. (a) XPS N1s spectra and of Ni-NC, $Ni_{66}Fe_{34}$-NC, Fe-NC, and Zn-NC. XPS fine scans on the (b) $Ni2p^{3/2}$ spectra and (c) $Fe2p^{3/2}$ spectra of Ni_xFe_{1-x}-NC (x = 100, 91, 80, 66, 43, 20, and 0). (d) Fe and (e) Ni K-edge XANES spectra of $Ni_{66}Fe_{34}$-NC, Fe-NC and standard samples. Fourier transformation of the EXAFS spectra at R space of (f) Fe and (g) Ni K-edge for $Ni_{66}Fe_{34}$-NC, Fe-NC and standard samples. (h) The fitting of first two shell Fe-N, Fe-Ni and Ni-N, Ni-Fe coordination paths of Fourier transformations of EXAFS. (i) Summary of Bader charge distributions of Ni-N_4, Fe-N_4, and Ni(N_3)-Fe(N_3) moieties, inset shows the schematic structure for atomically dispersed $Ni_{66}Fe_{34}$-NC.

Ni_xFe_{100-x}-NC materials (x = 20, 43, 66, 80, and 91) exhibit contrary trends by showing high N contents of 14.7–16.0 at.% (Figure S5a and Table S1) and Zn contents of 1.47–2.39 at.%.

The heavy decorations of N and Zn (reaching total contents of 10.9–18.3 at.%) in carbon substrates can serve as efficient fencing and stabilizing components for the immoblization of Ni and Fe atoms [80].XPS fine scans on N1s spectra revealed that different ratios of Ni/ Fe species gave significant impact on the configurations of nitrogen species. With the increase of Fe doses, both the percentages of pyridinic and pyrrolic N species increase while the percentage of graphitic N species decrease, the highest total content of pyridinic and pyrrolic N reaches to 79.6 % in $Ni_{20}Fe_{80}$-NC material (Figure S5b, Fig. 2a, and Figure S5d-g). The configuration of N species in Ni/Fe-free Zn-NC material was also analyzed, as shown in Fig. 2a, the N species in Zn-NC overwhelmingly take graphitic N form (53.1 %) while the percentage of graphitic N species in Ni-NC is only 17.4 %. The significantly altered N configurations in different metal-promoted M-NC materials can be as- cribed to the catalytic role of Ni and Fe for deep carbonization while Zn is merely serving as node metal to link multiple nitrogen species

[81,82]. The Ni and Fe contents on the surface of Ni_xFe_{100-x}-NC mate- rials (x = 0, 20, 43, 66, 80, 91, and 100) are in good monotonous re- lationship with the dosages in raw materials, as shown in Figure S4 and Table S1. Approximately 1.92 at.% (corresponding to 7.95 wt.%) Fe in oxidative states can be introduced into Fe-NC while about 1.09 at.% (corresponding to 4.45 wt.%) Ni are presenting in oxidative states in $Ni_{91}Fe_9$-NC (Table S1). These high contents of atomic Ni and Fe in this study are among the best achievable values for atomic Fe and Ni [83–85]. XPS fine scans on the Ni2p and Fe2p spectra of Ni_xFe_{100-x}-NC materials were conducted and compared in Fig. 2b/c, respectively. The deconvolutions of Ni2p spectra centered at 856.7 and 854.7 eV can be respectively indexed to the $Ni2p^{3/2}$ branches of Ni^{2+} and Ni^{3+}, and the deconvolutions of Fe2p spectra centered at 709.9 and 713.4 eV can be respectively indexed to the $Fe2p^{3/2}$ branches of Fe^{2+} and Fe^{3+}. The Ni^{3+} species are overwhelmingly presented relative to Ni^{2+} while Fe^{3+} species are more contributed in Ni_xFe_{100-x}-NC with x smaller than 80. It is noticeable that the binding energy of both Ni2p and Fe2p states ex- hibit down-shifting trends when Ni and Fe co-exist (Fig. 2b/c). It is seemingly that under the circumstance of Fe concentration increasing,

more Ni^{3+} species tend to maintain lower valence, for instance, the Ni^{3+} state of $Ni_{20}Fe_{80}$-NC showed a binding energy down-shifting of 0.5 eV compared to that of $Ni_{91}Fe_9$-NC. Similarly, more Fe^{2+} species would be also engage reductive down-shifting of binding energy when increasing heterogeneous metal, i.e., Ni. A down-shifting of binding energy of 0.35 eV for Fe^{2+} state was observed in $Ni_{91}Fe_9$-NC relative to the $Ni_{20}Fe_{80}$-NC. Therefore, to intergratedly constructing binary NiFe-NC, the atomic Ni and Fe species are most likely developing very intimate relationship of strong electron coupling, which can be interpreted into the cooperative synergy between Ni and Fe atoms in multiple N coordinations [86].

In order to examine the local environment of Ni/Fe atoms in Ni_xFe_{100-x}-NC materials, the $Ni_{66}Fe_{34}$-NC catalyst was further characterized by using XAFS. The Fe/Ni K edge x-ray absorption near-edge structures (XANES) were compared with synthetic Fe-NC, standard Ni/FePc (Pc = Phthalocyanine), Ni-/Fe foil, and Ni-/Fe oxides samples (Fig. 2d/e). The XANES spectra of Ni of $Ni_{66}Fe_{34}$-NC is shown having the features between NiO and Ni foil, and very similar to the standard NiPc molecule, suggesting the average valence of Ni in $Ni_{66}Fe_{34}$-NC is between Ni(0) and Ni(II). Similarly, the Fe XANES spectra of $Ni_{66}Fe_{34}$-NC is close to the standard FePc molecule, indicating the average valence of Fe is between Fe(0) and Fe(III) [87]. Furthermore, the relatively high overlaps of XANES spectra of $Ni_{66}Fe_{34}$-NC with NiPc and FePc suggest that the Ni/Fe species in $Ni_{66}Fe_{34}$-NC possesses similar coordination paths with multiple pyridinic/pyrrolic N. Fig. 3f/g display the Fourier transform (FT) k^3-weighted $\chi(k)$ function of the extended X-ray absorption fine structure (EXAFS) spectra. The main peaks of the first shells of Fe and Ni in $Ni_{66}Fe_{34}$-NC verify the dominant presence of Fe-N and Ni-N coordination paths at 1.47 Å and 1.30 Å, similarly, that in Fe-NC shows larger Fe-NC coordination path at 1.49 Å (Figure S6a). No significant peak is observable in the $Ni_{66}Fe_{34}$-NC spectra corresponding to the Fe-Fe and Ni-Ni coordination paths, as compared with the Fe foil and Ni foil references. In order to identify the precise Ni-Fe coordination path, simulate a hypothesized bimetallic NiFe-nitrogen model based on EXAFS experimental spectrum and FT curve fitting. The calculated Ni-Fe paths are in good agreement with the experimental spectra (Fig. 2h). According to the fitting results summarized in Table S2, the coordination numbers of Fe-N and Fe-Ni were about 2.9 and 1, respectively. Based on the fitting curve in Fig. 2h and Figure S6c/d, the coordination numbers of Ni-N and Ni-Fe were about 2.8 and 0.7 (Table

S2), respectively, which confirm the coordinations of Ni-Fe dual site as the deduced structure in the inset of Fig. 2i [88–90]. We then performed the Bader effective charge distribution analyais on the deduced structure of $Ni(N_3)$-$Fe(N_3)$-C_n. Its charge density diagram was compared with those of Ni-N_4-C_n and Fe-N_4-C_n segments in Figure S7 and summarized in Fig. 2i. It is revealed that both the charge density of Fe (0.93) and Ni (0.53) in $Ni(N_3)$-$Fe(N_3)$-C_n are lower than that of corresponding metal in M-N_4-C_n (M = Fe-1.07 or Ni-0.82), which is in accordance with XPS analysis that can be interpreted as more negative charge can localized at Ni-Fe dual site [91].

Furthermore, the Brunauer-Emmett-Teller (BET) specific surface area of the $Ni_{66}Fe_{34}$-NC was measured to be ~166 $m^2 g^{-1}$. The N_2 absorption/desorption isotherm curve (Figure S8a) and pore distribution curve (Figure S8b) confirm it mainly containing micropores and mesopores, which are respectively formed by Zn activation and particle stacking. Formation of hierarchial pores is of great benefit for mass transportation and exposure of larger active surface [92]. Prior to all electrocatalytic measurements, the electrochemical surface area (ECSA) of all the atomically dispersed bimetallic Ni_xFe_{100-x}-NC materials were evaluated, and Figure S9a displayed the plots of scan rate versus current density. The $Ni_{66}Fe_{34}$-NC obtains the largest ECSA of 14.6 m F cm^{-2}, indicating the largest electrochemically accessible active area exposed. A clear trend of larger exposed ECSA facilitated by bimetallic sources over single-metal source was observed. All the ECSA for bimetallic Ni_xFe_{100-x}-NC materials are close to or above 10 m F cm^{-2} while the ECSA for Ni- or Fe-NC material is typically ~5 m F cm^{-2}, rendering a feasible strategy of enlarging electrochemically exposed area by means of introducing multiple metal sources for forming pores in carbonaceous materials [93,94]. The Ni_xFe_{100-x}-NC were submitted to electrochemical measurements of evaluating ORR and OER performance. Initially, ORR polarization curves of all samples were collected in O_2-saturated 0.1 M KOH with a rotation speed of 1600 rpm. As shown in Figure S9b, higher onset and half-wave potentials are obtainable with the increases of Fe content, indicating that Fe species are the probable active sites for ORR. The catalytic activity, in terms of ORR onset and half-wave potentials, exhibits very limited increment after reaching the 40 % Fe, corresponds to 0.48 at.% and 1.99 wt.% Fe. Meanwhile, the OER polarization curves, as compared in Figure S10a, reveal a volcanic trend that consists of increasing and decreasing branches separated at
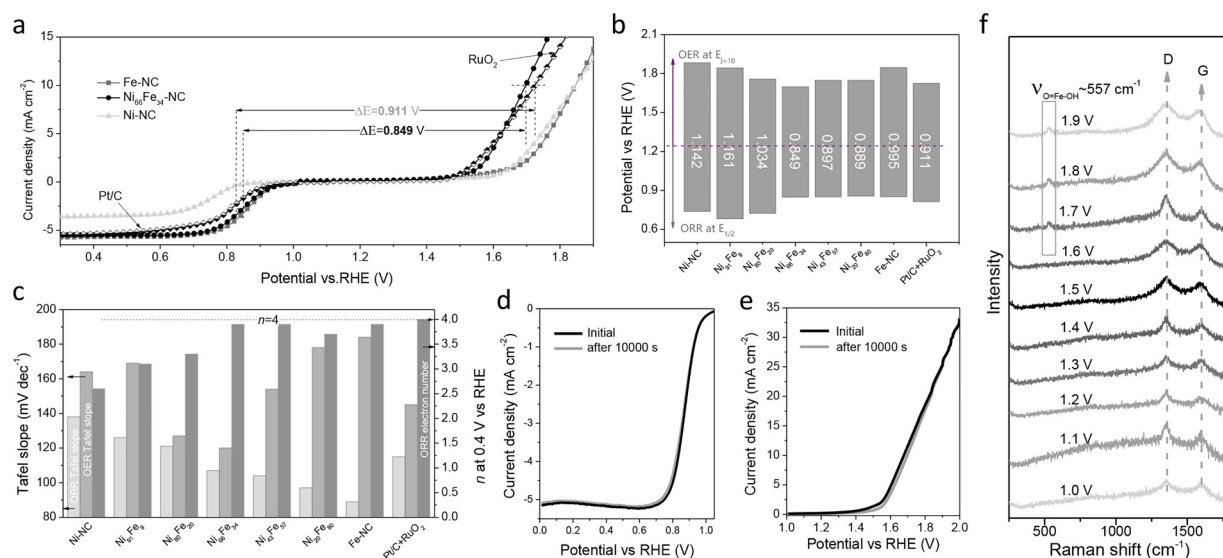

Fig. 3. (a) Combined ORR and OER polarization curves of Ni-NC, $Ni_{66}Fe_{34}$-NC, Fe-NC, and Pt/C-RuO$_2$ in O$_2$-saturated 0.1 mol L^{-1} KOH solution. (b) Comparison of potential gap (ΔE) between ORR half-wave potential ($^{ORR}E_{1/2}$) and OER potential at current density of 10.0 mA cm^{-2} ($^{OER}E_{j10}$) for all Ni_xFe_{100-x}-NC materials and Pt/C + RuO$_2$ reference. (c) Summaries on ORR and OER Tafel slopes and transfer electron number of all Ni_xFe_{100-x}-NC materials and Pt/C + RuO$_2$. (d) ORR and (e) OER polarization curve before and after 10000-second-long working at 0.67 V and 1.60 V, respectively. (f) *In-situ* Raman characterizations of $Ni_{66}Fe_{34}$-NC in O$_2$-saturated 0.1 M KOH with a three-electrode setup, the applied potentials were referred to reversible hydrogen electrode (RHE).
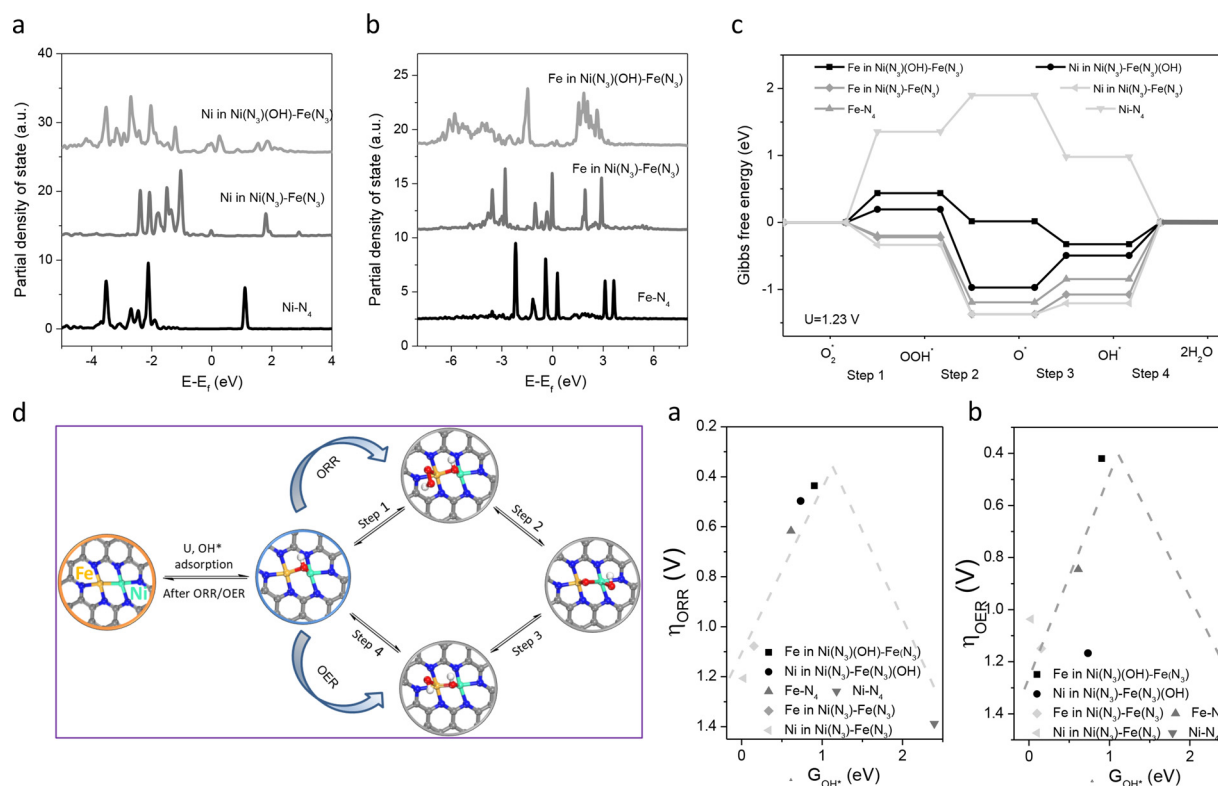
Fig. 4. (a) Fe3d and (b) Ni3d Partial density of state (PDOS) curves of Fe (or Ni)-N_4-C_n, $Ni(N_3)$-$Fe(N_3)$-C_n, and $Ni(N_3)(OH)$-$Fe(N_3)$-C_n. (c) Reaction free energy diagrams of possible responsible sites for ORR and OER (U = 1.23), including single metal Fe or Ni-N_4-C_n, Ni or Fe on bimetal $Ni(N_3)$-$Fe(N_3)$-C_n, and Ni or Fe on Ni (N_3)-$Fe(N_3)$-C_n with the other metal atom saturated by OH. The reaction pathways for ORR listed in this panel are Step 1: $O_2(g)$ + * + $H_2O(l)$ + e– ↔ OOH* + OH^-; Step 2: OOH* + e– ↔ O* + OH^-; Step 3: O* + $H_2O(l)$ + e– ↔ OH* + OH^-; and Step 4: OH* + e– ↔ * + OH^-, OER occurs inversely from step 4 to step 1. (d) Proposed ORR and OER mechanism on the Fe site in $Ni(N_3)(OH)$-$Fe(N_3)$-C_n, the $Ni(N_3)(OH)$-$Fe(N_3)$-C_n is evolved from the adsorption of OH on Ni in $Ni(N_3)$-$Fe(N_3)$-C_n moiety upon potential applied. The details of Step 1-4 in this panel are illustrated in panel (c). Volcano plots for (e) ORR and (f) OER on the abovementioned possible sites with a descriptor of ΔG_{OH*}.

x = 66. It shows the best onset potential of 1.51 V and the smallest overpotential of 467 mV to reach the current density (*j*) of 10.0 mA cm^{-2} in 0.1 M KOH. Furthermore, the activity descriptor in terms of potential gap (ΔE) between ORR half-wave potential ($^{ORR}E_{1/2}$) and OER potential at $j = 10.0$ mA cm^{-2} ($^{OER}E_{j=10}$) was investigated. Particularly, the $Ni_{66}Fe_{34}$-NC sample exhibits the smallest potential gap window by means of 0.848 V among all the Ni_xFe_{100-x}-NC samples (Fig. 3a/b), which is 61 mV lower than that of Pt/C-RuO_2 mixture. The volcanic trend of OER activity is inheritable into the ΔE variation by showing ΔE decreasing first then increasing along with Ni decreasing, suggesting the cooperative effect between atomic Ni and Fe for optimal ORR and OER performance [95–98].

The transfer electron number (*n*) of ORR processes and Tafel slopes for ORR and OER promoted by Ni_xFe_{100-x}-NC materials were calculated (Figure S9c/d and Figure S10b). As comparatively shown in Fig. 3c, the *n* of Ni_xFe_{100-x}-NC samples remain constantly close to 4 until the sto-chiometry (x) reached to 66, while further increasing the stochiometric value of x (i.e., more Ni content) results in the decrease of *n*. This trend once again suggests that the atomicallly dispersed Fe species are highly possible active sites for ORR [99].The ORR Tafel slopes for Ni_xFe_{100-x}-NC were also found with an increasing trend following the increases of Fe contents and ORR activities. In contrast, the OER Tafel slopes show a trend of decreasing to 120 mV dec^{-1} at x = 66 and then increasing with the increase of Ni content. The lowest Tafel slopes were achieved by $Ni_{66}Fe_{34}$-NC material: 107 mV dec^{-1} for ORR and 120 mV dec^{-1} for OER. While the standard Pt/C and RuO_2 show Tafel slopes of 115 mV dec^{-1} for ORR and 145 mV dec^{-1} for OER, respectively, implying highly efficient ORR/OER processes promoted by $Ni_{66}Fe_{34}$-NC.

The $Ni_{66}Fe_{34}$-NC was further subjected to the investigations of

cycling stability and tolerance to organic contaminant. Firstly, the methanol tolerance test was performed on the $Ni_{66}Fe_{34}$-NC and Pt/C electrocatalysts (Figure S9e). Results show that the $Ni_{66}Fe_{34}$-NC ex-hibits very limited flactuation of current response, as compared, Pt/C shows considerable activity loss over 48 %. The long-term stability of the catalysts was evaluated by using chronoamperometry measure-ments at -0.6 V and 1.7 V for ORR and OER, respectively. The activity losses of $Ni_{66}Fe_{34}$-NC for ORR and OER after long-term working (10000 s) are approximately ~2.5 % and ~10.7 %, respectively. In contrast, Pt/C show 22.7 % ORR activity loss, confirming the robustness of the $Ni_{66}Fe_{34}$-NC catalyst for long-term use (Fig. 3d/e and Figure S9f). Furthermore, *in-situ* Raman characterizations was performed on $Ni_{66}Fe_{34}$-NC to get in-depth insight into the responsible sites for OER. Fig. 3f displays the Raman spectra of $Ni_{66}Fe_{34}$-NC in 0.1 M KOH elec-trolyte upon different potential applied. As can be seen, a new band located at 557 cm^{-1} emerges when the applied potential reaches 1.7 V (versus RHE), which is indexed to one characteristic peak of FeOOH [100], suggesting the Fe site rather than Ni site is responsible for OER. Our finding is consistent with the previous reports regarding the co-operative Ni-Fe dual sites in NiFe-layered double hydroxide (LDH), in which Ni site may serve as mediator to optimize the properties of ad-jacent Fe site [101]. By normalizing kinetic current density with cor-responding electrochemical double-layer capacitance (EDLC), we can qualitatively assess the origin of improvement on catalytic perfor-mance. The bar chart in Figure S11a compares the kinetic current density after normalization sharply increases at Ni/Fe ratio of 66/34 and gradually increased thereafter, which confirms the critical role of Fe component for ORR catalysis. Similarly, OER current density was also normalized to their EDLC, as shown in Figure S11b, at lower

potential like 1.6–1.7 V, increasing Fe/Ni to 34/66 obtained the largest OER current density, further increasing Fe dosage sees the decrease of OER current density, which implies the cooperative effects between Ni and Fe.

In order to elucidate the beneficial role of dual-site Ni/Fe in $Ni_{66}Fe_{34}$-NC for ORR/OER, we conducted a combined theoretical investigation of spin-polarized DFT and VASP. The partial density of states (PDOS) of Ni and Fe on $Ni(N_3)$-$Fe(N_3)$-C_n moiety with comparison of Fe on Fe-N_4-C_n moiety and Ni on Ni-N_4-C_n moiety were simulated. As shown in Fig. 4a/b, in dual-site $Ni(N_3)$-$Fe(N_3)$, the Fe3d orbitals shifted to higher energy relative to those in Fe-N_4 while on the contrary, the Ni3d orbitals shifted to lower energy relative to those in Ni-N_4. The aforementioned information clearly indicated the strong synergy between Ni and Fe sites and high binding affinity of Ni sites towards the O-containing reactants and intermediates than Fe sites in dual-site $Ni(N_3)$-$Fe(N_3)$ [102–105]. Meanwhile, our experimental observation of *in-situ* Raman showed that Fe sites should be main catalytic active sites instead of Ni sites, leaving a further task to assist the roles of neighbor Ni site for the enhancement in ORR activity at Fe sites. It is well known that in alkaline media, the responsible catalytic site in M-N-C electrocatalysts binds with OH to facilitate the ORR as earlier reports [106–108]. Therefore, we further simulated the partial density of states (PDOS) of Ni and Fe on $Ni(N_3)$-$Fe(N_3)$-C_n moiety with OH saturated Ni sites, as shown in Figure S12. The OH group was found to be spontaneously bridge between Ni and Fe sites, forming a unique geometry of $Ni(N_3)$-$O(H)$-$Fe(N_3)$. After Ni/Fe sites bound with one OH, both the 3d orbitals of Ni and Fe sites exhibited considerable negative shift, implying the strength of those sites which bind with O-containing reactants and intermediates having significantly lowered, which favors the association/dissociation of OOH* [109].This fact can be correlated with the HOMO-LUMO theory which stated that the shifting of HOMO towards the Fermi level (E_f) cause the enhancement in the local electronic conductivity. Therefore, OH bridging between Ni and Fe modified the electronic structure of the catalytic active sites via charge transfer over the catalyst interface [110].

Further, the profiles of Gibbs free energy change (ΔG) with an external potential of 1.23 V were calculated on the following catalytic sites including Ni-N_4, Fe-N_4, Ni site in $Ni(N_3)$-$Fe(N_3)$, Fe site in $Ni(N_3)$-$Fe(N_3)$, Ni site in $Ni(N_3)$-$Fe(N_3)(OH)$, and Fe site in $Ni(N_3)$-(OH)-$Fe(N_3)$. Generally, ORR/OER reactions consist of four elementary steps that involve the five activated molecular states OH*, O*, OOH*, O_2* and H_2O (Fig. 4c). In the four-step reaction of ORR or OER, the rate-determining step (RDS), that is the elementary step with the largest ΔG, is key to evaluate the catalytic activity of specific site. As indicated in Fig. 4c and Table S3, the RDS on the Fe site in Fe-N_4, Ni site in $Ni(N_3)$-$Fe(N_3)$, Fe site in $Ni(N_3)$-$Fe(N_3)$, and Ni site in $Ni(N_3)$-$Fe(N_3)(OH)$ is the elementary step of OOH* + e– ↔ O* + OH^-. While, the Ni in Ni-N_4 and Fe site in $Ni(N_3)(OH)$-$Fe(N_3)$ followed the $O_2(g)$ + * + $H_2O(l)$ + e– ↔ OOH* + OH^- as RDS step. However, the energy barrier of Fe site in $Ni(N_3)(OH)$-$Fe(N_3)$ is 0.43 eV which is significantly lower than that of Ni in Ni-N_4 (1.35 eV), implying the Fe site in $Ni(N_3)(OH)$-$Fe(N_3)$ possesses the modest adsorption property for the O-containing intermediates among all measured cases. Specifically, Fe site in $Ni(N_3)(OH)$-$Fe(N_3)$ shows the smallest ΔG for the association/dissociation of OOH. Meanwhile, unlike other five sites, the absolute values of ΔG of the four elementary steps on Fe site in $Ni(N_3)(OH)$-$Fe(N_3)$ are all smaller than 0.44 eV, implying excellent catalytic properties of reversibly converting O_2 and OH^- [39,111].

In details, Fig. 4d shows the geometry of each intermediates on Fe site in $Ni(N_3)(OH)$-$Fe(N_3)$ during the bifunctional oxygen catalysis, the geometry of reaction intermediates on other sites are included in Figure S13. Specifically, for ORR processes, OH act as bridge between Ni and Fe under the potential driving force, then O_2 molecule adsorbs on Fe site and OH solely coordinates the adjacent Ni site [112], further steps of the formation/dissociation of OOH*, and the formation/desorption of OH are all occurred on Fe site with neighboring OH-saturated Ni site.

Further, the energy barriers of ORR/OER processes promoted on the abovementioned sites were calculated, Fe sites in Ni site in Fe-N_4, Ni (N_3)-$Fe(N_3)$, and $Ni(N_3)(OH)$-$Fe(N_3)$ show energy barriers of 1.00, 1.15, and 0.44 eV, respectively, and Ni sites in Ni site in Ni-N_4, $Ni(N_3)$-$Fe(N_3)$, and $Ni(N_3)$-$Fe(N_3)(OH)$ show energy barriers of 1.35, 0.96, and 1.17 eV, respectively. The overpotentials of ORR/OER on each catalytic site were calculated based on the largest energy barriers in four steps. A nearly linear relationship was established between $\triangle G_{OH*}$ and the overpotentials (η) of ORR and OER on the abovementioned active sites except Ni-N_4, as shown in Fig. 4e/f. The Fe site in $Ni(N_3)(OH)$-$Fe(N_3)$ is revealed having the lowest overpotential for both ORR and OER, which are respectively 0.436 V and 0.420 V and both values are reaching at the tops of volcano plots of $\triangle G_{OH*}$-η. In contrast, the overpotentials for ORR and OER occurring on Fe-N4 are 0.617 V and 0.814 V, respectively which are much higher that former $Ni(N_3)(OH)$-$Fe(N_3)$, confirming the beneficial role of adjacent Ni in boosting the bifunctional oxygen electrocatalytic activities.

In addition, rechargeable Zn-air battery (ZAB) was built up by using $Ni_{66}Fe_{34}$-NC-assembled air cathode to evaluate the bifunctionality of the catalyst ($Ni_{66}Fe_{34}$-NC) for the downstream applications. Zn foil was used as anode and a mixture of Pt/C and RuO_2 (1:1 w/w) was used as a reference cathode material. Initially, the $Ni_{66}Fe_{34}$-NC delivers an open circuit voltage (OCV) as high as 1.44 V after 300 min standing, 60 mV higher than Pt/C-RuO_2 driven ZAB (Fig. 5a). Upon used as primary ZAB with $j = 10.0$ mA cm^{-2}, the $Ni_{66}Fe_{34}$-NC initially exhibits a 1.22-V discharging voltage, ~210 mV higher than that of Pt/C-RuO_2. The discharge voltage of $Ni_{66}Fe_{34}$-NC -assembled primary ZAB can still maintain at 1.17 V high at cell approaching end under current density of 10.0 mA cm^{-2} (Fig. 5b). Fig. 5c displays the variations in charge/discharge voltage and specific power of the $Ni_{66}Fe_{34}$-NC and Pt/C-RuO_2 catalysts plotting to j. The $Ni_{66}Fe_{34}$-NC exhibits a maximum power density of 140.1 mW cm^{-2} at $j = 234.4$ mA cm^{-2} while the Pt/C-RuO_2 shows a maximum power density of 111.3 mW cm^{-2} at much lower $j = 174.7$ mA cm^{-2}. Furthermore, the rate performance on both charging/discharging were compared at different j from 1 to 20 mA cm^{-2} with time interval of 1 h (Fig. 5d). The potential gap between discharge and charge potentials for the $Ni_{66}Fe_{34}$-NC catalyst can be lowered down to 0.69 V at $j = 1$ mA cm^{-2}, delivering the 1.22-V discharge voltage and 1.91-V charge voltage. The potential gap gradually grows up to 1.04 V at 20 mA cm^{-2} for $Ni_{66}Fe_{34}$-NC, consisting a 1.05-V discharge voltage and a 2.00-V charge voltage. In contrast, the Pt/C-RuO_2 exhibits a 1.18-V discharge voltage and 1.98-V charge voltage at $j = 1$ mA cm^{-2}, but it posseses much lower discharge voltage of 0.92 V and higher charge voltage of 2.16 V at $j = 20$ mA cm^{-2}. Moreover, the $Ni_{66}Fe_{34}$-NC catalyst can be effectively used for 1000 cycles at both low rates (1.0, 5.0, and 10.0 mA cm^{-2}, Figure S14) and high rate (20.0 mA cm^{-2}, Fig. 5e). Both the discharge/charge voltages can be well-maintained in a 334 -h long-term cycling. However, the Pt/C-RuO_2 catalyst suffers significant decrease of discharge voltage and increase of charge voltage under $j = 20.0$ mA cm^{-2}. Its charge voltage skyrockets to 2.5 V and discharge voltage down to 0.76 V at the 50th cycle.

4. Conclusions

In conclusion, a feasible method to build atomically dispersed binary NiFe-NC materials with tunable Ni/Fe ratios was established for achieving optimal bifunctional ORR/OER performance. The optimally synthesized $Ni_{66}Fe_{34}$-NC material, as confirmed by EXAFS and its fitting, contains large amount of $Ni(N_3)$-$Fe(N_3)$-C_n moieties in which Ni and Fe form dual-site geometry that allow more negative charge localized at Ni and Fe sites. Electrochemical measurement showed that the $Ni_{66}Fe_{34}$-NC material possessed superior bifunctional oxygen electrocatalytic performance in alkaline media, delievering high ORR half-wave potential of 0.85 V and low OER overpotential of 467 mV at 10 mA cm^{-2}. Moreover, the $Ni_{66}Fe_{34}$-NC-assembled Zn-air battery afforded a large power density, robust rate performance, and

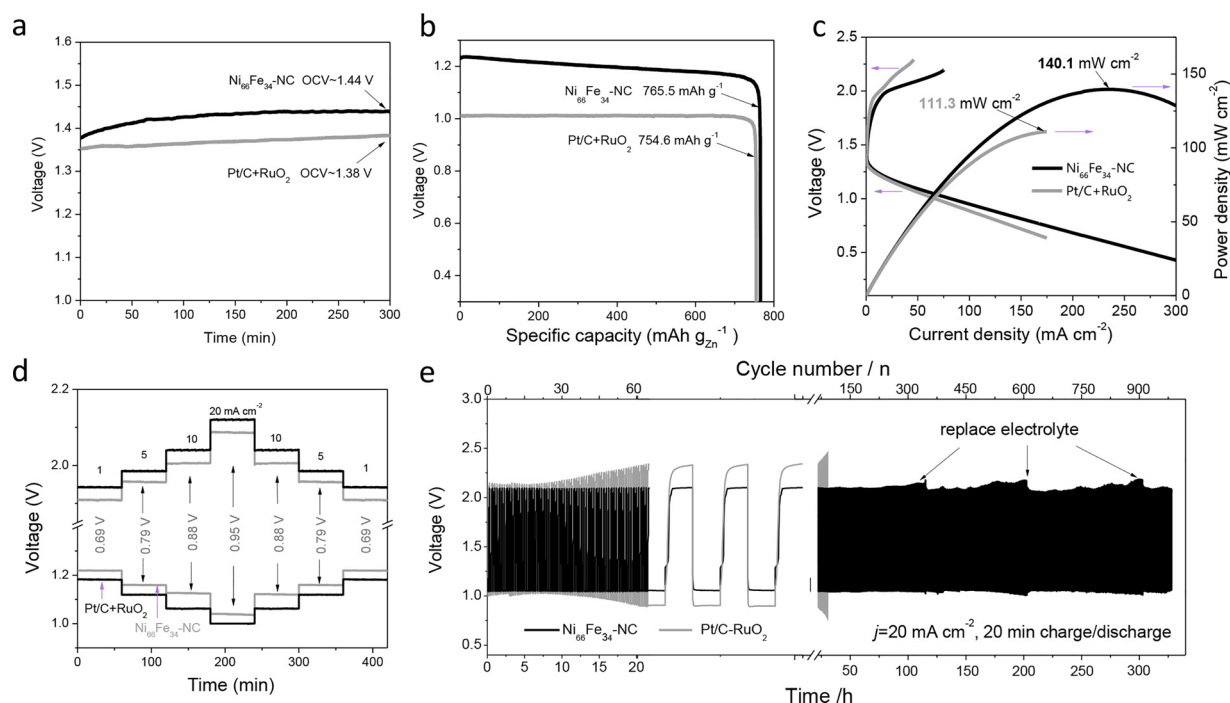**Fig. 5.** Evaluations of Zn-air battery performance on $Ni_{66}Fe_{34}$-NC- and Pt/C-RuO$_2$-assembled air cathode. (a) Open-circuit voltage measurements, (b) Specific capacity measured at a current density of 10.0 mA cm^{-2}. Charge/discharge polarization curves and power densities. (d) Galvanostatic charge and discharge polarization plots at different current densities. (e) Long-term cycling performance with current density of 20.0 mA cm^{-2}.

extraordinary cycling stability. Furthermore, the *in-situ* Raman characterizations and DFT computations indicated the Fe site in $Ni(N_3)(OH)$-$Fe(N_3)$ was the responsible site for both ORR and OER. As suggested, the neighbored Ni site with the coordination of OH served as excellent mediator to adjust the properties of Fe site for efficient formation, association, and dissociation of OOH*. The calculated overpotentials of Fe site in $Ni(N_3)(OH)$-$Fe(N_3)$ for ORR and OER can be significantly lowered to 0.436 V and 0.420 V, respectively. We believe may work for many potentially open the reliable ways for further design of multiple atomically dispersed metal-nitrogen-carbon materials with cooperative active metal centers for broad efficient electrocatalytic reactions.

CRediT authorship contribution statement

Mang Ma: Software, Data curation, Investigation, Writing - original draft. **Anuj Kumar:** Investigation, Writing - review & editing. **Danni Wang:** Methodology, Visualization. **Yiyan Wang:** Writing - review & editing, Investigation. **Yin Jia:** Supervision, Data curation. **Ying Zhang:** Writing - review & editing. **Guoxin Zhang:** Conceptualization, Methodology, Writing - review & editing, Funding acquisition. **Zifeng Yan:** Writing - review & editing. **Xiaoming Sun:** Supervision, Writing - review & editing, Project administration.

Declaration of Competing Interest

The authors declare that they have no known competing financial interests or personal relationships that could have appeared to influence the work reported in this paper.

Acknowledgements

Appendix A. Supplementary data

Supplementary material related to this article can be found, in the online version, at doi:https://doi.org/10.1016/j.apcatb.2020.119091.

References

[1] T. Ioroi, Z. Siroma, S.i. Yamazaki, K. Yasuda, Adv. Energy Mater. 9 (23) (2019) 1801284.
[2] D.Scamman Staffell, A. Velazquez Abad, P. Balcombe, P.E. Dodds, P. Ekins, N. Shah, K.R. Ward, Energy Environ. Sci. 12 (2) (2019) 463–491.
[3] H.J. Qiu, P. Du, K. Hu, J. Gao, H. Li, P. Liu, T. Ina, K. Ohara, Y. Ito, M. Chen, Adv. Mater. 31 (19) (2019) 1900843.
[4] Y. Huang, Y. Wang, C. Tang, J. Wang, Q. Zhang, Y. Wang, J. Zhang, Adv. Mater. 31 (13) (2019) 1803800.
[5] M. Faustini, M. Giraud, D. Jones, J. Rozière, M. Dupont, T.R. Porter, S. Nowak, M. Bahri, O. Ersen, C. Sanchez, C. Boissière, C. Tard, J. Peron, Adv. Energy Mater. 9 (4) (2019) 1802136.
[6] Q. Feng, Z. Zhao, X.-Z. Yuan, H. Li, H. Wang, Appl. Catal. B 260 (2020) 118176.
[7] S.K. Singh, K. Takeyasu, J. Nakamura, Adv. Mater. 31 (13) (2018) 1804297.
[8] J.-C. Dong, X.-G. Zhang, V. Briega-Martos, X. Jin, J. Yang, S. Chen, Z.-L. Yang, D.-Y. Wu, J.M. Feliu, C.T. Williams, Z.-Q. Tian, J.-F. Li, Nat. Energy 4 (1) (2018) 60–67.
[9] W. Zhou, D.D. Huang, Y.P. Wu, J. Zhao, T. Wu, J. Zhang, D.S. Li, C. Sun, P. Feng, X. Bu, Angew. Chem. Int. Ed. Engl. 58 (13) (2019) 4227–4231.
[10] H. Jiang, Q. He, X. Li, X. Su, Y. Zhang, S. Chen, S. Zhang, G. Zhang, J. Jiang, Y. Luo, P.M. Ajayan, L. Song, Adv. Mater. 31 (8) (2019) 1805127.
[11] D. Gao, R. Liu, J. Biskupek, U. Kaiser, Y.F. Song, C. Streb, Angew. Chem. Int. Ed. Engl. 58 (14) (2019) 4644–4648.
[12] F. Lyu, Q. Wang, S.M. Choi, Y. Yin, Small 15 (1) (2019) 1804201.
[13] J. Liu, Q. Ma, Z. Huang, G. Liu, H. Zhang, Adv. Mater. 31 (9) (2019) 1800696.
[14] Z. Pu, J. Zhao, I.S. Amiinu, W. Li, M. Wang, D. He, S. Mu, Energy Environ. Sci. 12 (3) (2019) 952–957.
[15] Y. Fan, F. Ma, J. Liang, X. Chen, Z. Miao, S. Duan, L. Wang, T. Wang, J. Han, R. Cao, S. Jiao, Q. Li, Nanoscale 12 (2) (2020) 584–590.
[16] Y. Du, F.-X. Ma, C.-Y. Xu, J. Yu, D. Li, Y. Feng, L. Zhen, Nano Energy 61 (2019)

533–539.

[17] J. Li, M. Chen, D.A. Cullen, S. Hwang, M. Wang, B. Li, K. Liu, S. Karakalos, M. Lucero, H. Zhang, C. Lei, H. Xu, G.E. Sterbinsky, Z. Feng, D. Su, K.L. More, G. Wang, Z. Wang, G. Wu, Nat. Catal. 1 (12) (2018) 935–945.

[18] H. Wu, H. Li, X. Zhao, Q. Liu, J. Wang, J. Xiao, S. Xie, R. Si, F. Yang, S. Miao, X. Guo, G. Wang, X. Bao, Energy Environ. Sci. 9 (12) (2016) 3736–3745.

[19] Z. Zhang, J. Sun, F. Wang, L. Dai, Angew. Chem. Int. Ed. Engl. 57 (29) (2018) 9038–9043.

[20] Y. Zheng, Y. Jiao, Y. Zhu, Q. Cai, A. Vasileff, L.H. Li, Y. Han, Y. Chen, S.Z. Qiao, J. Am. Chem. Soc. 139 (9) (2017) 3336–3339.

[21] C. Zhu, S. Fu, Q. Shi, D. Du, Y. Lin, Angew. Chem. Int. Ed. Engl. 56 (45) (2017) 13944–13960.

[22] S. Yuan, Z. Pu, H. Zhou, J. Yu, I.S. Amiinu, J. Zhu, Q. Liang, J. Yang, D. He, Z. Hu, G. Van Tendeloo, S. Mu, Nano Energy 59 (2019) 472–480.

[23] H.J. Qiu, Y. Ito, W. Cong, Y. Tan, P. Liu, A. Hirata, T. Fujita, Z. Tang, M. Chen, Angew. Chem. Int. Ed. Engl. 54 (47) (2015) 14031–14035.

[24] W. Chen, J. Pei, C.T. He, J. Wan, H. Ren, Y. Zhu, Y. Wang, J. Dong, S. Tian, W.C. Cheong, S. Lu, L. Zheng, X. Zheng, W. Yan, Z. Zhuang, C. Chen, Q. Peng, D. Wang, Y. Li, Angew. Chem. Int. Ed. Engl. 56 (50) (2017) 16086–16090.

[25] H.B. Yang, S.-F. Hung, S. Liu, K. Yuan, S. Miao, L. Zhang, X. Huang, H.-Y. Wang, W. Cai, R. Chen, J. Gao, X. Yang, W. Chen, Y. Huang, H.M. Chen, C.M. Li, T. Zhang, B. Liu, Nat. Energy 3 (2) (2018) 140–147.

[26] W. Ren, X. Tan, W. Yang, C. Jia, S. Xu, K. Wang, S.C. Smith, C. Zhao, Angew. Chem. Int. Ed. Engl. 58 (21) (2019) 6972–6976.

[27] X.F. Li, Q.K. Li, J. Cheng, L. Liu, Q. Yan, Y. Wu, X.H. Zhang, Z.Y. Wang, Q. Qiu, Y. Luo, J. Am. Chem. Soc. 138 (28) (2016) 8706–8709.

[28] H. Tao, C. Choi, L.-X. Ding, Z. Jiang, Z. Han, M. Jia, Q. Fan, Y. Gao, H. Wang, A.W. Robertson, S. Hong, Y. Jung, S. Liu, Z. Sun, Chem 5 (1) (2019) 204–214.

[29] W. Yang, W. Yang, L. Dong, X. Gao, G. Wang, G. Shao, J. Mater. Chem. A 7 (21) (2019) 13103–13112.

[30] L. Ma, H. Lin, W. Zhang, P. Zhao, G. Zhu, Y. Hu, R. Chen, Z. Tie, J. Liu, Z. Jin, Nano Lett. 18 (12) (2018) 7949–7954.

[31] R. Zhang, X.R. Chen, X. Chen, X.B. Cheng, X.Q. Zhang, C. Yan, Q. Zhang, Angew. Chem. Int. Ed. Engl. 56 (27) (2017) 7764–7768.

[32] Q. Jia, E. Liu, L. Jiao, S. Pann, S. Mukerjee, Adv. Mater. 31 (31) (2019) 1805157.

[33] H. Chen, K. Shen, Y. Tan, Y. Li, ACS Nano 13 (7) (2019) 7800–7810.

[34] Y. Sun, L. Silvioli, N.R. Sahraie, W. Ju, J. Li, A. Zitolo, S. Li, A. Bagger, L. Arnarson, X. Wang, T. Moeller, D. Bernsmeier, J. Rossmeisl, F. Jaouen, P. Strasser, J. Am. Chem. Soc. 141 (31) (2019) 12372–12381.

[35] H. Yang, X. Chen, W.T. Chen, Q. Wang, N.C. Cuello, A. Nafady, A.M. Al-Enizi, G.I.N. Waterhouse, G.A. Goenaga, T.A. Zawodzinski, P.E. Kruger, J.E. Clements, J. Zhang, H. Tian, S.G. Telfer, S. Ma, ACS Nano 13 (7) (2019) 8087–8098.

[36] C. Guo, W. Liao, Z. Li, L. Sun, H. Ruan, Q. Wu, Q. Luo, J. Huang, C. Chen, Chin. Sci. Bull. 61 (12) (2016) 948–958.

[37] L. Liu, J. Zhang, W. Ma, Y. Huang, Sci. China Mater. 62 (3) (2018) 359–367.

[38] Z.-F. Huang, J. Song, Y. Du, S. Xi, S. Dou, J.M.V. Nsanzimana, C. Wang, Z.J. Xu, X. Wang, Nat. Energy 4 (4) (2019) 329–338.

[39] M.A. Hunter, J.M.T.A. Fischer, Q. Yuan, M. Hankel, D.J. Searles, ACS Catal. 9 (9) (2019) 7660–7667.

[40] J. Li, S. Chen, N. Yang, M. Deng, S. Ibraheem, J. Deng, J. Li, L. Li, Z. Wei, Angew. Chem. Int. Ed. Engl. 58 (21) (2019) 7035–7039.

[41] H. Jin, X. Feng, J. Li, M. Li, Y. Xia, Y. Yuan, C. Yang, B. Dai, Z. Lin, J. Wang, J. Lu, S. Wang, Angew. Chem. Int. Ed. Engl. 58 (8) (2019) 2397–2401.

[42] K. Gao, B. Wang, L. Tao, B.V. Cunning, Z. Zhang, S. Wang, R.S. Ruoff, L. Qu, Adv. Mater. 31 (13) (2019) 1805121.

[43] J. Ortiz-Medina, Z. Wang, R. Cruz-Silva, A. Morelos-Gomez, F. Wang, X. Yao, M. Terrones, M. Endo, Adv. Mater. 31 (13) (2019) 1805717.

[44] L. An, B. Huang, Y. Zhang, R. Wang, N. Zhang, T. Dai, P. Xi, C.H. Yan, Angew. Chem. Int. Ed. Engl. 58 (28) (2019) 9459–9463.

[45] L. Zhang, R. Si, H. Liu, N. Chen, Q. Wang, K. Adair, Z. Wang, J. Chen, Z. Song, J. Li, M.N. Banis, R. Li, T.K. Sham, M. Gu, L.M. Liu, G.A. Botton, X. Sun, Nat. Commun. 10 (1) (2019) 1–11.

[46] S.L. Zhang, B.Y. Guan, X.W.D. Lou, Small 15 (13) (2019) 1805324.

[47] S. Li, C. Cheng, X. Zhao, J. Schmidt, A. Thomas, Angew. Chem. Int. Ed. Engl. 57 (7) (2018) 1856–1862.

[48] J. Wang, W. Liu, G. Luo, Z. Li, C. Zhao, H. Zhang, M. Zhu, Q. Xu, X. Wang, C. Zhao, Y. Qu, Z. Yang, T. Yao, Y. Li, Y. Lin, Y. Wu, Y. Li, Energy Environ. Sci. 11 (12) (2018) 3375–3379.

[49] Y. Pan, S. Liu, K. Sun, X. Chen, B. Wang, K. Wu, X. Cao, W.C. Cheong, R. Shen, A. Han, Z. Chen, L. Zheng, J. Luo, Y. Lin, Y. Liu, D. Wang, Q. Peng, Q. Zhang, C. Chen, Y. Li, Angew. Chem. Int. Ed. Engl. 57 (28) (2018) 8614–8618.

[50] F. Yang, J. Ye, Q. Yuan, X. Yang, Z. Xie, F. Zhao, Z. Zhou, L. Gu, X. Wang, Adv. Funct. Mater. 30 (11) (2020) 1908235.

[51] H. Lv, L. Sun, D. Xu, Y. Ma, B. Liu, Appl. Catal. B 253 (2019) 271–277.

[52] C. Li, M. Wu, R. Liu, Appl. Catal. B 244 (2019) 150–158.

[53] X. Wang, X. Xu, C. Niu, J. Meng, M. Huang, X. Liu, Z. Liu, L. Mai, Nano Lett. 17 (1) (2017) 544–550.

[54] E. Hu, X.-Y. Yu, F. Chen, Y. Wu, Y. Hu, X.W.D. Lou, Adv. Energy Mater. 8 (9) (2018) 1702476.

[55] Z. Meng, S. Cai, R. Wang, H. Tang, S. Song, P. Tsiakaras, Appl. Catal. B 244 (2019) 120–127.

[56] E. Hu, Y. Feng, J. Nai, D. Zhao, Y. Hu, X.W. Lou, Energy Environ. Sci. 11 (4) (2018) 872–880.

[57] S.-H. Bae, J.-E. Kim, H. Randriamahazaka, S.-Y. Moon, J.-Y. Park, I.-K. Oh, Adv. Energy Mater. 7 (1) (2017) 1601492.

[58] J. Nai, Y. Lu, L. Yu, X. Wang, X.W.D. Lou, Adv. Mater. 29 (41) (2017).

[59] J.F.G. Kresse, Comput. Mater. Sci. 6 (1996) 15–50.

[60] G. Kresse, J. Furthmüller, Phys. Rev. B 54 (16) (1996) 11169.

[61] V.V. Anisimov, J. Zaanen, O.K. Andersen, Phys. Rev. B Condens. Matter 44 (3) (1991) 943–954.

[62] G. Kresse, D. Joubert, J. Phys. Rev. B. 59 (3) (1999) 1758.

[63] J.P. Perdew, K. Burke, M. Ernzerhof, Phys. Rev. Lett. 77 (18) (1996) 3865.

[64] J. Ma, L. Gong, Y. Shen, D. Sun, B. Liu, J. Zhang, D. Liu, L. Zhang, Z. Xia, Front. Mater. 6 (2019) 294.

[65] Z. Zhao, Z. Xia, ACS Catal. 6 (3) (2016) 1553–1558.

[66] I.C. Man, H.Y. Su, F. Calle-Vallejo, H.A. Hansen, J.I. Martínez, N.G. Inoglu, J. Kitchin, T.F. Jaramillo, J.K. Nørskov, J. Rossmeisl, ChemCatChem 3 (7) (2011) 1159–1165.

[67] J.K. Nørskov, J. Rossmeisl, A. Logadottir, L.R.K.J. Lindqvist, J.R. Kitchin, T. Bligaard, et al., J. Phys. Chem. B 108 (2004) 17886–17892.

[68] G. Zhang, Y. Jia, C. Zhang, X. Xiong, K. Sun, R. Chen, W. Chen, Y. Kuang, L. Zheng, H. Tang, W. Liu, J. Liu, X. Sun, W.-F. Lin, H. Dai, Energy Environ. Sci. 12 (4) (2019) 1317–1325.

[69] H. Zhang, S. Hwang, M. Wang, Z. Feng, S. Karakalos, L. Luo, Z. Qiao, X. Xie, C. Wang, D. Su, Y. Shao, G. Wu, J. Am. Chem. Soc. 139 (40) (2017) 14143–14149.

[70] S. Wei, A. Li, J.C. Liu, Z. Li, W. Chen, Y. Gong, Q. Zhang, W.C. Cheong, Y. Wang, L. Zheng, H. Xiao, C. Chen, D. Wang, Q. Peng, L. Gu, X. Han, J. Li, Y. Li, Nat. Nanotechnol. 13 (9) (2018) 856–861.

[71] Y. Zhu, W. Sun, J. Luo, W. Chen, T. Cao, L. Zheng, J. Dong, J. Zhang, M. Zhang, Y. Han, C. Chen, Q. Peng, D. Wang, Y. Li, Nat. Commun. 9 (1) (2018) 1–9.

[72] Y. Qu, Z. Li, W. Chen, Y. Lin, T. Yuan, Z. Yang, C. Zhao, C. Zhao, X. Wang, F. Zhou, Z. Zhuang, Y. Wu, Y. Li, Nat. Catal. 1 (10) (2018) 781–786.

[73] X. Xiong, Y. Li, Y. Jia, Y. Meng, K. Sun, L. Zheng, G. Zhang, Y. Li, X. Sun, Nanoscale 11 (34) (2019) 15900–15906.

[74] Z. Lu, B. Wang, Y. Hu, W. Liu, Y. Zhao, R. Yang, Z. Li, J. Luo, B. Chi, Z. Jiang, M. Li, S. Mu, S. Liao, J. Zhang, X. Sun, Angew. Chem. Int. Ed. Engl. 58 (9) (2019) 2622–2626.

[75] Z. Du, X. Chen, W. Hu, C. Chuang, S. Xie, A. Hu, W. Yan, X. Kong, X. Wu, H. Ji, L.J. Wan, J. Am. Chem. Soc. 141 (9) (2019) 3977–3985.

[76] Z. Tan, H. Li, Q. Feng, L. Jiang, H. Pan, Z. Huang, Q. Zhou, H. Zhou, S. Ma, Y. Kuang, J. Mater. Chem. A 7 (4) (2019) 1607–1615.

[77] P. Yin, T. Yao, Y. Wu, L. Zheng, Y. Lin, W. Liu, H. Ju, J. Zhu, X. Hong, Z. Deng, G. Zhou, S. Wei, Y. Li, Angew. Chem. Int. Ed. Engl. 55 (36) (2016) 10800–10805.

[78] Q. Wang, L. Shang, R. Shi, X. Zhang, G.I.N. Waterhouse, L.-Z. Wu, C.-H. Tung, T. Zhang, Nano Energy 40 (2017) 382–389.

[79] H. Jiang, J. Gu, X. Zheng, M. Liu, X. Qiu, L. Wang, W. Li, Z. Chen, X. Ji, J. Li, Energy Environ. Sci. 12 (1) (2019) 322–333.

[80] G. Wu, A. Santandreu, W. Kellogg, S. Gupta, O. Ogoke, H. Zhang, H.-L. Wang, L. Dai, Nano Energy 29 (2016) 83–110.

[81] H. Wang, Q. Wang, Y. Cheng, K. Li, Y. Yao, Q. Zhang, C. Dong, P. Wang, U. Schwingenschlogl, W. Yang, X.X. Zhang, Nano Lett. 12 (1) (2012) 141–144.

[82] K. Chi, Z. Chen, F. Xiao, W. Guo, W. Xi, J. Liu, H. Yan, Z. Zhang, J. Xiao, J. Liu, J. Luo, S. Wang, K.P. Loh, J. Mater. Chem. A 7 (26) (2019) 15575–15579.

[83] J.-C. Li, M. Cheng, T. Li, L. Ma, X. Ruan, D. Liu, H.-M. Cheng, C. Liu, D. Du, Z. Wei, Y. Lin, M. Shao, J. Mater. Chem. A 7 (24) (2019) 14478–14482.

[84] Y. Cheng, S. Zhao, H. Li, S. He, J.-P. Veder, B. Johannessen, J. Xiao, S. Lu, J. Pan, M.F. Chisholm, S.-Z. Yang, C. Liu, J.G. Chen, S.P. Jiang, Appl. Catal. B 243 (2019) 294–303.

[85] K. Yang, Y. Liu, J. Deng, X. Zhao, J. Yang, Z. Han, Z. Hou, H. Dai, Appl. Catal. B 244 (2019) 650–659.

[86] C.-S.H. Jun Gu, Lichen Bai, HaoMing Chen, Hu Xile, Science 364 (6445) (2019) 1091–1094.

[87] C. Zhao, X. Dai, T. Yao, W. Chen, X. Wang, J. Wang, J. Yang, S. Wei, Y. Wu, Y. Li, J. Am. Chem. Soc. 139 (24) (2017) 8078–8081.

[88] A. Zitolo, V. Goellner, V. Armel, M.T. Sougrati, T. Mineva, L. Stievano, E. Fonda, F. Jaouen, Nat. Mater. 14 (9) (2015) 937–942.

[89] C. Yan, H. Li, Y. Ye, H. Wu, F. Cai, R. Si, J. Xiao, S. Miao, S. Xie, F. Yang, Y. Li, G. Wang, X. Bao, Energy Environ. Sci. 11 (5) (2018) 1204–1210.

[90] J. Wang, Z. Huang, W. Liu, C. Chang, H. Tang, Z. Li, W. Chen, C. Jia, T. Yao, S. Wei, Y. Wu, Y. Li, J. Am. Chem. Soc. 139 (48) (2017) 17281–17284.

[91] Y. Zhou, Z. Wang, Z. Pan, L. Liu, J. Xi, X. Luo, Y. Shen, Adv. Mater. 31 (8) (2019) 1806769.

[92] P. He, X.Y. Yu, X.W. Lou, Angew. Chem. Int. Ed. Engl. 56 (14) (2017) 3897–3900.

[93] C. Zhang, J. Sha, H. Fei, M. Liu, S. Yazdi, J. Zhang, Q. Zhong, X. Zou, N. Zhao, H. Yu, Z. Jiang, E. Ringe, B.I. Yakobson, J. Dong, D. Chen, J.M. Tour, ACS Nano 11 (7) (2017) 6930–6941.

[94] X. Wang, Z. Li, Y. Qu, T. Yuan, W. Wang, Y. Wu, Y. Li, Chem 5 (6) (2019) 1486–1511.

[95] Y. Cheng, S. He, J.P. Veder, R. De Marco, Sz. Yang, S. Ping Jiang, ChemElectroChem 6 (13) (2019) 3478–3487.

[96] C. Kuai, Y. Zhang, D. Wu, D. Sokaras, L. Mu, S. Spence, D. Nordlund, F. Lin, X.-W. Du, ACS Catal. 9 (7) (2019) 6027–6032.

[97] C. Wu, X. Zhang, Z. Xia, M. Shu, H. Li, X. Xu, R. Si, A.I. Rykov, J. Wang, S. Yu, S. Wang, G. Sun, J. Mater. Chem. A 7 (23) (2019) 14001–14010.

[98] Y. Feng, Q. Shao, Y. Ji, X. Cui, Y. Li, X. Zhu, X. Huang, Sci. Adv. 4 (7) (2018) eaap8817.

[99] X. Wang, H. Zhang, H. Lin, S. Gupta, C. Wang, Z. Tao, H. Fu, T. Wang, J. Zheng, G. Wu, X. Li, Nano Energy 25 (2016) 110–119.

[100] X. Wang, M. Ta, T. Edvinsson, Nano Energy 66 (2019) 104118.

[101] K. Zhu, X. Zhu, W. Yang, Angew. Chem. Int. Ed. Engl. 58 (5) (2019) 1252–1265.

[102] H. Zhang, Y. Liu, T. Chen, J. Zhang, J. Zhang, X.W.D. Lou, Adv. Mater. 31 (48) (2019) 1904548.

[103] C.Y. Lin, L. Zhang, Z. Zhao, Z. Xia, Adv. Mater. 29 (17) (2017) 1606635.
[104] H. Zhang, W. Zhou, T. Chen, B.Y. Guan, Z. Li, X.W. Lou, Energy Environ. Sci. 11 (8) (2018) 1980–1984.
[105] H. Zhang, W. Zhou, J. Dong, X.F. Lu, X.W. Lou, Energy Environ. Sci. 12 (11) (2019) 3348–3355.
[106] A. Kumar, Y. Zhang, W. Liu, X. Sun, Coord. Chem. Rev. 402 (2020) 213047.
[107] X. Zhao, X. Liu, B. Huang, P. Wang, Y. Pei, J. Mater. Chem. A 7 (42) (2019) 24583–24593.
[108] M. Xiao, L. Gao, Y. Wang, X. Wang, J. Zhu, Z. Jin, C. Liu, H. Chen, G. Li, J. Ge,

[109] Q. He, Z. Wu, Z. Chen, W. Xing, J. Am. Chem. Soc. 141 (50) (2019) 19800–19806.
[109] Y. Zhou, S. Sun, J. Song, S. Xi, B. Chen, Y. Du, A.C. Fisher, F. Cheng, X. Wang, H. Zhang, Z.J. Xu, Adv. Mater. 30 (32) (2018) 1802912.
[110] J. Zhang, Y. Zhao, C. Chen, Y.C. Huang, C.L. Dong, C.J. Chen, R.S. Liu, C. Wang, K. Yan, Y. Li, G. Wang, J. Am. Chem. Soc. 141 (51) (2019) 20118–20126.
[111] J.C. Liu, X.L. Ma, Y. Li, Y.G. Wang, H. Xiao, J. Li, Nat. Commun. 9 (1) (2018) 1–9.
[112] X. Li, H. Wang, Z. Cui, Y. Li, S. Xin, J. Zhou, Y. Long, C. Jin, J.B. Goodenough, Sci. Adv. 5 (8) (2019) eaav6262.